

High-latitude MSTIDs over the EISCAT-3D site: Solar activity and seasonal dependency

Rahul Rathi¹, Adrian Grocott¹, Tim K. Yeoman², Mark Lester²

¹Lancaster University, Lancaster, United Kingdom

²University of Leicester School of Physics and Astronomy, Leicester, UK

Correspondence: Adrian Grocott (a.grocott@lancaster.ac.uk)

Abstract. This work involves an investigation of high-latitude medium scale traveling ionospheric disturbances (MSTIDs) over the newly established EISCAT-3D radar site. We have used the ground backscatter data from an HF radar located at Hankasalmi, Finland (~62.3°N, ~26.61°E geographic coordinates), which is a part of the SuperDARN (Super Dual Auroral Radar Network). Data from solar maximum (2001 & 2014) and minimum (1996 & 2009) years from solar cycles 23 and 24 have been used to investigate the characteristics, seasonal variation, and possible generating sources of high-latitude daytime MSTIDs. Irrespective of the seasons and solar activity conditions, a dominant fraction of MSTIDs propagates equatorward with velocity in the range of 50 – 150 m s⁻¹ and period in the range of 30 – 60 minutes. Their occurrence shows seasonal and solar activity dependency. They normally occur during winter and equinoctial months. During solar maximum conditions, the occurrence is comparatively higher (~72 %) than during solar minimum years (below 50 %). Furthermore, the MSTIDs' occurrence shows a dependence on IMF Bz, being generally higher during intervals of prolonged northward or southward IMF Bz, and lower during small or fluctuating IMF Bz conditions. Our results indicate that MSTIDs occurrence shows seasonal variation as well as dependence on the solar forcing. Therefore, this statistical study will help in providing comprehensive insight about the MSTIDs which will be effective in scheduling future experimental runs of EISCAT-3D to explore their 3-dimensional structures.

1. Introduction

Traveling ionospheric disturbances (TIDs) are propagating electron density perturbations in the ionosphere. They pose a persistent challenge due to their ability to severely affect radio propagation, often leading to disruption of radio-communications, increased convergence time of the precise point positioning of Global Navigation Satellite Systems (GNSS), and distortion of radio signals from astronomical sources (Boyde et al., 2025; Carter et al., 2023; Maletckii & Astafyeva, 2024). They are believed to be the manifestation of atmospheric gravity waves (Hines, 1960; Hocke & Schlegel, 1996; Hunsucker, 1982). Based on their scale sizes, TIDs are categorized as large, medium, and small scale (Hunsucker, 1982). Large scale TIDs (LSTIDs) having wavelengths of more than 1000 km, propagate towards the equator with a velocity in the range of 400-1000 m s⁻¹, have a period of more than 1 hour and are mostly generated by geomagnetic activity in the auroral region (Ding et al., 2008; Tsugawa et al., 2004). Small scale TIDs (SSTIDs) have wavelengths less than 100 km and are usually generated by lower atmospheric gravity waves (Boyde et al., 2022). Medium scale TIDs (MSTIDs) normally propagate equatorward with a velocity of a few hundred m s⁻¹, a period in the range of 30 – 60 minutes, and wavelength of a few hundred km (Grocott et al., 2013; Hocke & Schlegel, 1996; Huang et al., 2016; Ishida et al., 2008; Rathi et al., 2025;

30 Shiokawa et al., 2003) and are believed to be generated by various sources (e.g., external solar forcing, internal atmospheric forcing, and natural hazards).

MSTIDs have been observed and reported over both mid and high-latitude regions (Grocott et al., 2013; Huang et al., 2016; Ishida et al., 2008; Shiokawa et al., 2003). Mid-latitude MSTIDs have been investigated extensively, and observations indicate that they generally occur during geomagnetic quiet time (Ding et al., 2011; 35 Huang et al., 2016), whereas MSTIDs over high latitudes occur during both geomagnetic quiet and active times. They are believed to be generated by multiple sources such as Joule heating by geomagnetic storms and substorms, gravity waves generated by tropospheric convection, and the solar terminator (Grocott et al., 2013; Ishida et al., 2008; Prikryl et al., 2022 & 2024). There are studies which explored high-latitude MSTIDs utilizing datasets from various ground and satellite-based instruments over both hemispheres (Frissell et al., 2016; Grocott et al., 2013; 40 Ishida et al., 2008; Negale et al., 2018; Ogawa et al., 1987; Prikryl et al., 2022 & 2024; Shiokawa et al., 2013; Vlasov et al., 2011; Xiong et al., 2025). These studies reported MSTIDs that normally propagate towards the equator and whose occurrence shows seasonal variation. However, a lack of agreement exists in the observed seasonal dependence; with peak occurrence in both summer (Vlasov et al., 2011) and winter (Moges et al., 2024a; Negale et al., 2018; Ogawa et al., 1987) months. In addition, there are two schools of thought on their generation 45 with respect to geomagnetic activity. There are studies which reported high-latitude MSTIDs during geomagnetic quiet and/or moderately disturbed times and suggested that the occurrence of these MSTIDs did not increase with increasing geomagnetic activity (Frissell et al., 2016; Ishida et al., 2008; Ogawa et al., 1987). On the other hand, Prikryl et al. (2022 & 2024) reported that MSTIDs over high-latitudes can also be generated by atmospheric gravity waves induced through Joule heating by external solar forcing (geomagnetic storms and/or substorms). 50 More recently, Xiong et al. (2025) reported that high-latitude daytime MSTIDs can also be observed during prolonged northward IMF Bz conditions and explored the possible role of intermittent lobe reconnection behind their generation. It is thus very apparent that a wide variety of generation or seeding mechanisms are associated with high-latitude MSTIDs. However, there is still much uncertainty surrounding their seasonal variation and the conditions that make a particular mechanism dominant.

55 This study aims to explore the seasonal variation and generating sources of the high-latitude MSTIDs using ground backscatter data of the Hankasalmi radar. The rationale behind selecting the Hankasalmi radar is the geographic location and the operational range that coincides partially with the newly established EISCAT-3D radar. EISCAT-3D is the most advanced high power three-dimensional imaging radar for atmospheric, ionospheric, and near-Earth space investigations. Since it requires high power and high cost for experimental runs, 60 a prior understanding of ionospheric irregularities (e.g., their characteristics, occurrence patterns with respect to season and external solar forcing) is required before its operational phase. In order to deepen our understanding, we have investigated daytime MSTIDs during solar maximum (2001 & 2009) and minimum years (1996 & 2009) from solar cycles 23 – 24 over this region and have used different approaches to characterize the observed MSTIDs while also investigating the role of external solar forcing behind their occurrence.

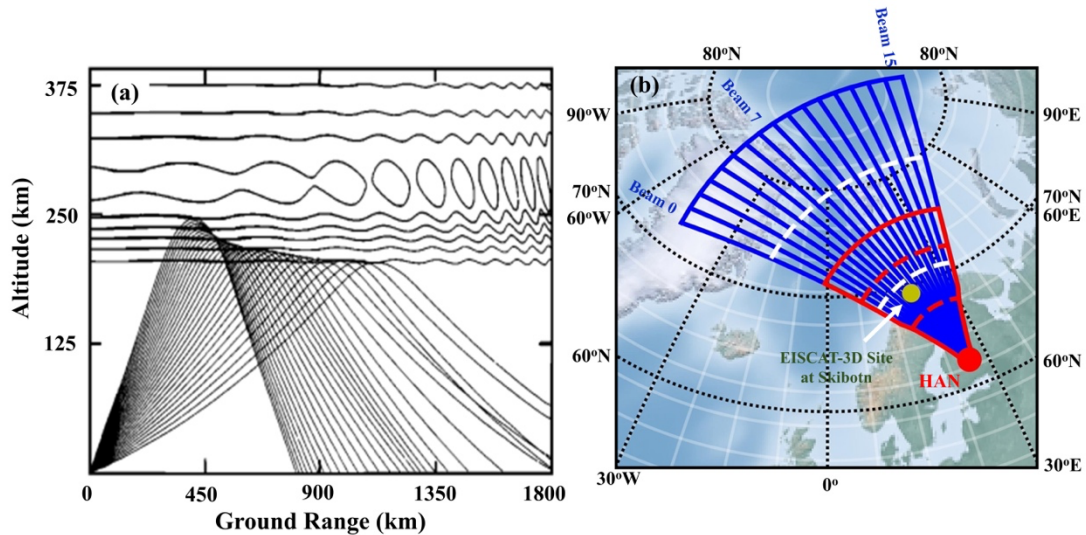
65

2. Instruments, Data, and Analyses Methods

In the present study, we have used the data from an HF radar located at Hankasalmi, Finland (~62.3°N, ~26.61°E geographic coordinates). The Hankasalmi radar (hereafter HAN) is a part of the SuperDARN (Super Dual Auroral

70 Radar Network), an international array of coherent radars in the Northern and Southern Hemispheres (Greenwald et al., 1995; Chisham et al., 2007). In the normal mode of operation, the HAN radar uses 16 beams for scanning with azimuthal separation of 3.24° , where each beam typically consists of 75 range gates of size 45 km, with the first range gate sampling at 180 km from the radar location (for a full field of view thus spanning ~ 3500 km). Each beam typically has a dwell time of ~ 3 sec and thus the radar completes a full 16 beam scan in ~ 1 minute (in the initial phase of operation the radar had dwell time of ~ 7 sec with a full scan in ~ 2 minutes).

75 A SuperDARN radar works on the principle of coherent scattering and receives backscatter signals from the ionosphere as well as from the ground. Such radars receive ionospheric backscatter if the transmitted signal intersects with the ionospheric target orthogonally to the magnetic field (achieved through ionospheric refraction of the signal). Further refraction of the signals directs the transmitted signals to the ground, from which they can propagate back to the radar. This is known as ground backscatter (GBS). Modulations/fluctuations in ionospheric
80 plasma density caused by MSTIDs affect the GBS by focussing/defocussing of the signals (Grocott et al., 2013; Samson et al., 1989 & 1990) as shown in Figure 1a. It is apparent from the figure that the location of the TID signature in GBS will be displaced from its actual location at the ionospheric height. Therefore, we have mapped the GBS to the ionosphere using the standard geolocation functions in the pyDARN python library (SuperDARN Data Visualization Working Group, 2025) to estimate the location of the observed MSTIDs. The field of view (FOV) of the HAN radar in GBS ranges is represented by the blue FAN plot whereas the red FAN plot represents the mapped ionospheric ranges in Figure 1b. The location of the HAN radar and EISCAT-3D at Skibotn, Norway are represented by the red and yellow dots, respectively. EISCAT-3D is located close to beam 7 (the nearly northward pointing beam) of the HAN radar. Therefore, in this study we have used data from beam 7 (as the central beam) in our analysis. We also restrict the analysis to radar range gates 20 – 45, which is the region where
85 the maximum amount of radar ground backscatter was observed. This region is confined between the white dashed curves (in GBS ranges) and red dashed curves (in mapped ranges) in Figure 1b.



95 **Figure 1.** (a) Model ray paths of HF propagation through a TID modulated ionosphere (adapted from Samson et al. (1990)). (b) Field of view (FOV) of HAN radar in GBS ranges (blue FAN plot) and ionospheric mapped ranges (red FAN plot). The red and yellow dots show the locations of the HAN radar and EISCAT-3D at Skibotn, respectively. HAN radar range gates 20 and 45 (bounding the area under study) are indicated by the white dashed (GBS ranges) and red dashed (mapped ranges) curves.

100 MSTIDs observed between 60° and 90° latitude are categorized as high-latitude MSTIDs. As the HAN radar probes the same ionospheric region (as shown by its FOV in Figure 1b), the main objective of this study is to investigate the propagation characteristics and occurrence of high-latitude MSTIDs during different solar activity conditions. We have therefore used HAN GBS data for solar minimum (1996 & 2009) and maximum (2001 & 2014) years from solar cycles 23 and 24. To determine the propagation characteristics, viz. velocity, period, and direction of propagation [azimuth angle (clockwise from geographic north)] of the observed MSTIDs in the GBS, the multichannel maximum entropy method (MULMEM) has been used (Grocott et al., 2013; Ishida et al., 2008; Shibata, 1987; Strand, 1977; Ulrych & Bishop, 1975). This method uses cross-spectral analysis to determine the parameters of MSTIDs from the GBS time series. We note that GBS depends on the ionospheric plasma density which reduces significantly during nighttime (Milan et al., 1997), therefore, the present study focusses on daytime MSTIDs observed in the GBS.

110 MSTIDs have periods of ~30 – 60 minutes, therefore, we have performed the MULMEM analysis on a window of 160 minutes, such that it covers at least 2 – 3 wave periods. The analysis is then performed across an 8-hour time series with the window shifted in 1 min increments. Each overlapping window segment produces a set of propagation parameters/characteristics [period, velocity and azimuth (clockwise from geographic north)] that is attributed to the centre time of the window, therefore with each slide of this window we build up a time-series of parameters. The MULMEM algorithm uses three time series from three radar cells (combination of beams and range gates) to determine these propagation characteristics of the observed MSTIDs. The location of EISCAT-3D at Skibotn lies within the beam 7 of HAN radar, therefore, in the present study we considered beam set (5, 7, 9). The range gates are chosen based on the region of higher GBS occurrence and it is seen that, during daytime, consistently higher GBS was observed between range gates 20 and 45. Therefore, our chosen combinations of the beam-range sets (cells) are [(5, r); (7, $r+4$); (9, r)], where r (range gates) varies from 20 to 45. To detect the existence of MSTIDs, the MULMEM method first checks whether the GBS time series data is continuous or not. A time series comprising non-continuous data is considered unfit to be processed further. After the initial check, the time series of period values is calculated using cross-spectral analysis and is followed by calculating the concordance rate, where the number of determined period values is divided by total data points in the time series of period. When the concordance rate is greater than 10% (to remove the cases with very few MSTID detections), the algorithm proceeds with the presence/existence of a TID. Once the presence of a TID in the time series is confirmed, the algorithm determines the propagation parameters/characteristics. Using cross spectral analysis, it determines the dominant period within the time window (160 minutes). In selecting the dominant period for each time window, it checks and only considers if the dominant period across all the three time windows is within ± 5 minutes. Then it evaluates the velocity and azimuth after estimating the separation and time delay between the cells. The window is then shifted and the cross-spectral analysis repeated. Ultimately, a set of three time-series of parameters is produced for each three-cell set, from which a mean time-series of parameters is derived for each cell set. To estimate the uncertainty of the parameters we have determined their standard deviation across the three time series for every MSTID event. The maximum uncertainty across the considered four years in period, velocity, and azimuth is observed to be 12%, 9.5%, and 9.8% of the respective average values. We further considered if the presence of a MSTID is detected in multiple three-cell sets. In those cases, we again checked the standard deviation of the parameters across all the cell sets at each time. For such cases where parameters show similar values (with standard deviation < 20%) for different cell sets, we consider

those as single MSTID events. Figure 2a shows an example (on 27 January 2014) of such cases where parameters are nearly the same in different cell sets and count as a single MSTID event.

140 A separate half an hour non-overlapping window is considered to check temporal variations in the parameters by assessing the mean and standard deviation of each window. Figure 2b is representative of this analysis, where average parameters for every half an hour window and their standard deviation (shown by error bars) are plotted for different cell sets. For the first cell set (first row of Figure 2b), two different values of the parameters are observed (marked with black rectangles) for different time ranges. In such scenarios, where parameters show two different values (azimuth difference $\geq 90^\circ$; velocity & period difference \geq double) either with time and/or different cell sets, we count them as two different MSTIDs. Also, we checked the standard deviation of each half an hour window and made sure it is less than 20% of the average value for each parameter. The number of such cases are few and in most of those cases MSTIDs are observed at different times. The cases where the parameters show high temporal variations/fluctuations (Azimuth $\geq 45^\circ$; Velocity $\geq 50 \text{ m s}^{-1}$; Period ≥ 15 minutes) with larger standard deviations ($\geq \pm 20\%$ of the values) and/or scattered values with time (as shown in second and third row of Figure 2b) are not considered/counted.

145
150
155
160
165
MSTIDs cause focussing/defocussing of SuperDARN GBS, therefore they appear as bands of high GBS. To confirm the presence of MSTIDs and their propagation, we have also checked the Range Time (RT) (e.g. Figure 3a) and FAN (which shows spatial coverage of GBS power across the radar's FOV, see Figure S1 in supporting information) plots for each case. In the present study we have visually inspected the RT plots for MSTID signatures and compared them with the results obtained from MULMEM. As mentioned above, due to the detection approach of MULMEM there are instances where the method failed to identify MSTIDs when cross checked with the RT plots (Table 1). We presume this is due to the requirement for a clear signal to be present in the 3 radar cells. In many of these cases, a signal was present in at least one cell, enabling a Fast Fourier Transform (FFT) analysis to determine a dominant period. For all the MSTID events observed in the RT plots we therefore also performed an FFT analysis to determine their period (using the same window size from the time series of beam 7) by selecting time series between the range gates 20 and 45 (as selected for MULMEM). Figure 3 shows an example MSTID (Figure 3a), and its parameters obtained from MULMEM (red curves in Figures 3b-d: velocity, azimuth angle, & period) & FFT (blue curve in Figure 3d: period). We have also provided a comparison of the MSTIDs detected using the MULMEM analysis, and the total number of MSTIDs observed in the RT plots for each year (see Table 1).

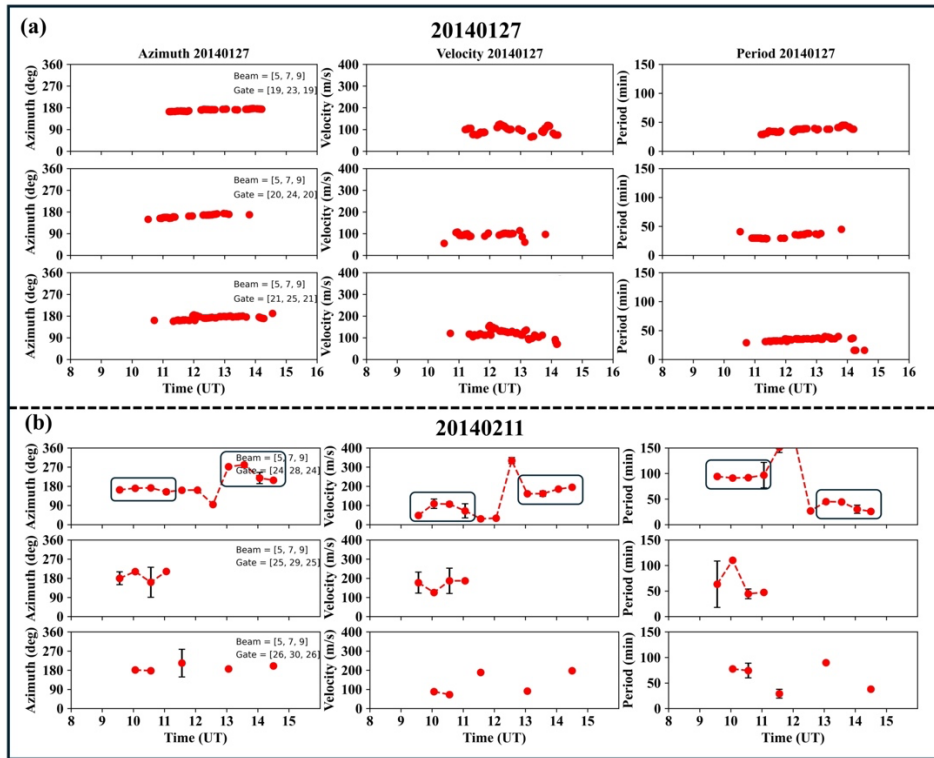
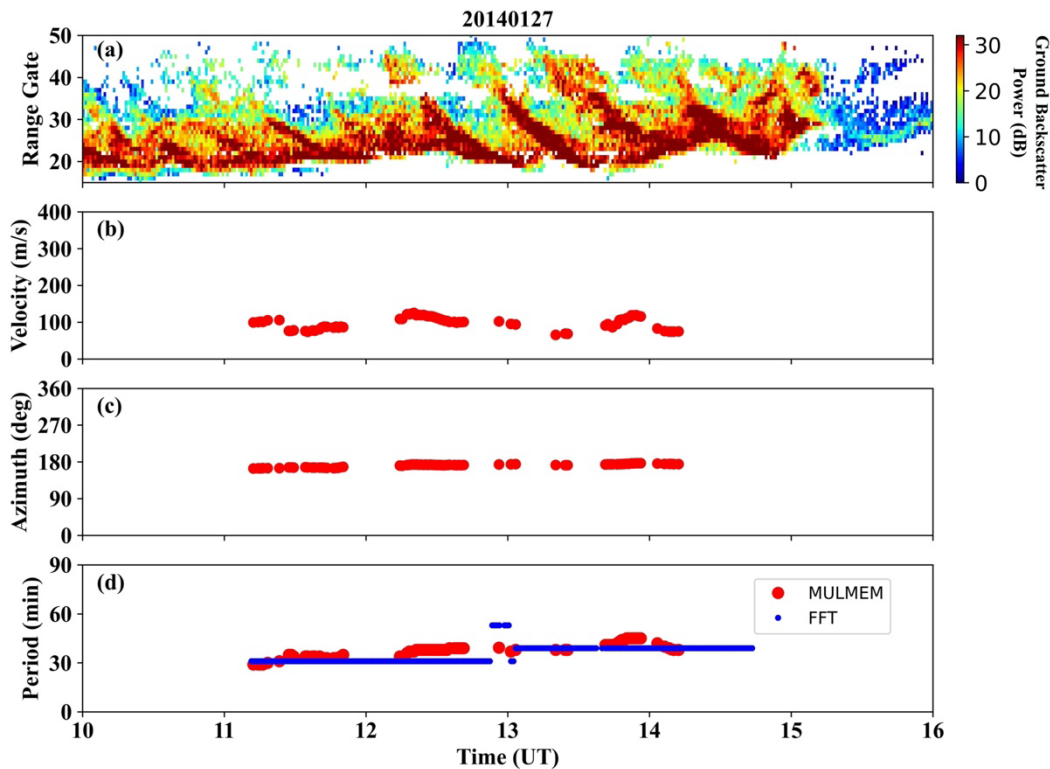


Figure 2. Parameters (azimuth, velocity, and period) determined using MULMEM for the MSTIDs observed on two different days; (a) on 27 January 2014 and (b) on 11 February 2014. [The black rectangles in subfigure \(b\) represents the parameters of two different MSTIDs observed on the same day.](#)



170 **Figure 3.** (a) An example showing MSTID in RT plot, (b-c) velocity and azimuth angle (clockwise from geographic north) determined using MULMEM, (d) comparison of period determined using MULMEM (red curve) and FFT (blue curve).

3. Results

175 This section presents a statistical overview of the high-latitude daytime MSTIDs observed during different solar activity conditions. As described in the previous section, we have applied different methods to detect and determine their characteristics. A detailed description about their occurrence and characteristics is given below.

3.1 Seasonal and solar activity dependence of MSTIDs' occurrence

180 As observed and reported earlier, SuperDARN GBS depends on a number of factors including the refraction and absorption of the transmitted signal, the occurrence of plasma structures, and the ionospheric density. In general, the higher the ionospheric density the greater will be the level [\(signal to noise ratio\) of GBS](#) (Milan et al., 1997). In the present study, due to higher ionospheric density in the daytime and thus higher GBS, we have considered the daytime observations from the HAN radar during the selected four years. As daytime extends for different
185 time lengths depending upon seasons, therefore, we have considered a fixed time window between 9 and 17 LT (close to the beam 7 observation region) across all seasons. Figure 4 shows the variation of monthly average F10.7 index, percentage occurrence of GBS, and MSTIDs percentage and relative occurrence. In each subfigure, the maroon and grey curves show the variation during solar maximum (dashed for 2001 & solid for 2014) and minimum (dashed for 1996 & solid for 2009) years, respectively. Figure 4a shows the monthly variation of F10.7
190 index, which was comparatively higher during solar maximum years (2001 & 2014) than during minimum years (1996 & 2009). Figure 4b shows the variation of the monthly percentage occurrence of daytime GBS of beam 7. The GBS monthly percentage occurrence was determined by dividing the number of bins (time and range gate bin) where GBS was present (GBS power > 0) by the total number of bins for time range 8 – 16 UT and range gate 20 – 45 for each day (when the radar was operating in its normal mode) of the respective month. It is to be
195 noted that, irrespective of the solar activity conditions, GBS occurrence across all the years shows a seasonal variation. GBS occurrence is comparatively higher in the winter and equinoctial months, but it reduces significantly in the summer. In addition to the seasonal variation, GBS occurrence shows a solar activity dependence. It is higher during the solar maximum years (maroon curves) than during the minimum years (grey curves). Figure 4c shows the monthly percentage occurrence of MSTIDs, calculated as the total number of days with MSTIDs activity observed in GBS for each month with respect to the total number of days the HAN radar was operational (in normal mode) for that particular month. The occurrence of MSTIDs shows a similar pattern to the GBS occurrence, with a significantly higher occurrence during solar maximum years, and during winter and equinoctial months, compared to solar minimum years and summer months. It can also be seen from Table 1 that the occurrence of MSTIDs is more than 70 % during solar maximum years (2001 & 2014), whereas it reduces
200 below 50 % during the solar minimum years (1996 & 2009). Figures 4b & c show that both GBS and MSTIDs occurrence exhibits seasonal variation. Therefore, there is a chance that the MSTID seasonal variation might have
205 [been](#) influenced by the GBS seasonal variation. We have thus determined the relative occurrence (see Figure 4d) of the MSTIDs with respect to GBS occurrence, which was determined by dividing the MSTIDs percentage occurrence for each month with the percentage occurrence of GBS for the respective month. It is interesting to
210 note that, similar to the GBS and MSTID occurrence, MSTIDs relative occurrence also shows a seasonal variation.

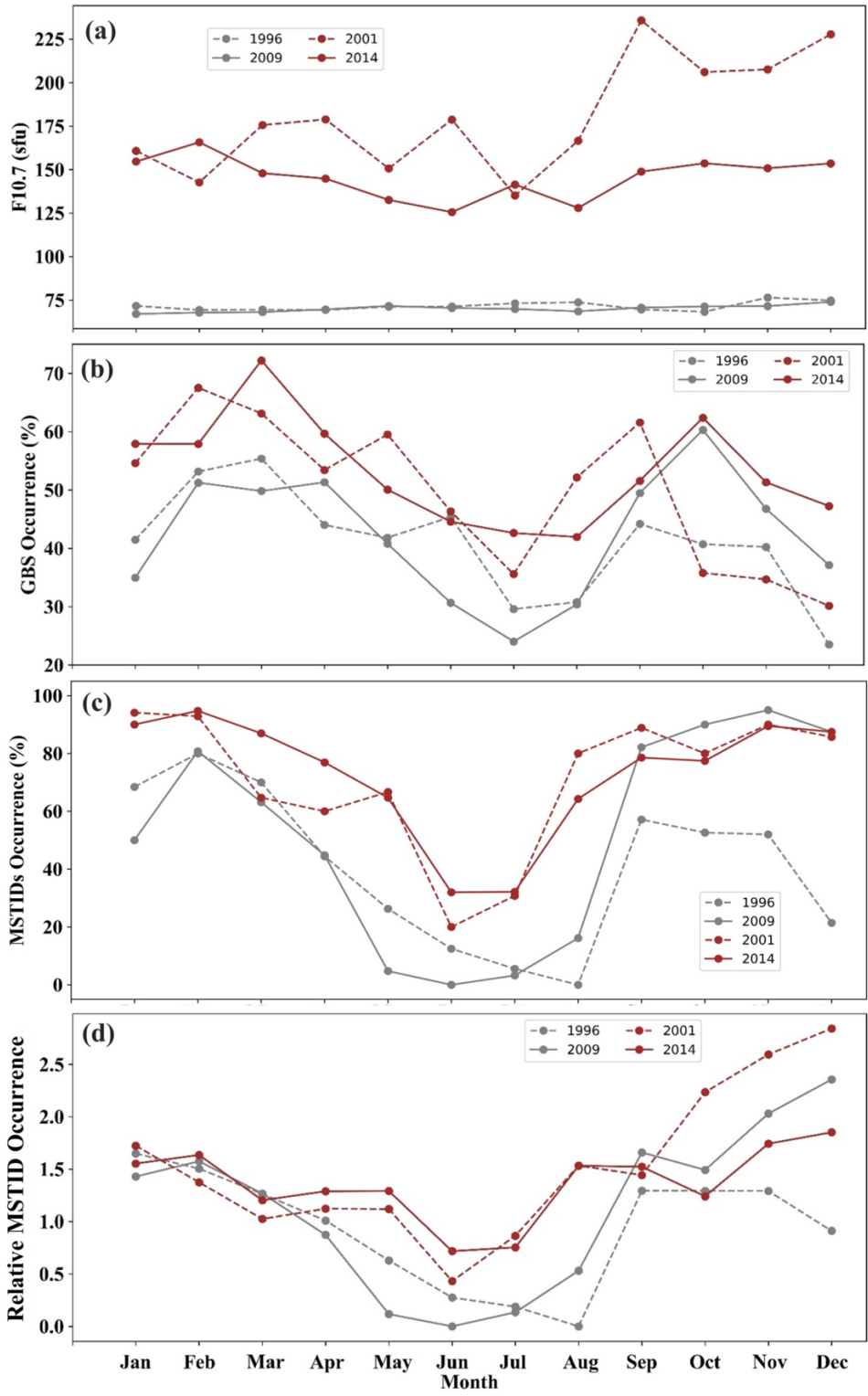


Figure 4. (a) Monthly average F10.7 index, (b) monthly % occurrence of ground backscatter, (c) monthly % occurrence of the MSTIDs, and (d) relative occurrence of MSTIDs with respect to GBS occurrence during solar minimum and maximum years of solar cycle 23 and 24.

215 **3.2 Characteristics of MSTIDs**

Figure 5 presents bar plots of the velocity and period distribution of the observed MSTIDs from the MULMEM and FFT analyses described above. The bar plots in brown & maroon show the MSTIDs' percentage occurrence

(obtained by dividing the number of MSTIDs in each group of velocity/period to the total number of MSTIDs observed in the respective year) during solar maximum years (2001 & 2014), whereas dark & light grey bars show MSTIDs during solar minimum years (1996 & 2009). Figure 5a shows the velocity distribution obtained using the MULMEM method, which is distributed in 5 velocity groups (0 – 50, 50 – 150, 150 – 250, 250 – 350, & above 350; in $m s^{-1}$). It can be inferred from the velocity distribution that irrespective of the solar activity conditions (across 4 years), ~60% of the MSTIDs propagates in the velocity range 50 – 150 $m s^{-1}$. The second dominant fraction (more than 20%) of MSTIDs propagates with velocity in the range of 150 – 250 $m s^{-1}$. Figures 5b-c show the period distribution determined using both MULMEM and FFT methods. This shows that irrespective of the methods and solar activity conditions, most of the MSTIDs have a period in the range of 30 – 60 minutes, whereas the second dominant fraction has a period in the range of 60 – 90 minutes.

Figure 6 shows the distribution of the azimuth angle of the observed MSTIDs. The azimuth is distributed in 8 groups with each group covering an angle range of 45 degrees (centred at 45, 90, 135, 180, 225, 270, 315, & 360 degrees). Each circle in the plots represents the magnitude of the velocity in an increasing order from the centre (each circle marked with the magnitude of the velocity in red font with 0 $m s^{-1}$ at the centre). The grey shaded areas represent the different azimuth ranges, and their extension represents the average velocity of the MSTIDs traveling in those directions. The numbers of MSTIDs traveling in each azimuth range are marked by the yellow font on each shaded area. We can infer that, regardless of the solar activity conditions, a dominant fraction of the observed MSTIDs propagates equatorward (southward) with a second dominant fraction propagating southeastward. There is a very small number of MSTIDs traveling towards north, east, and west. It is also interesting to note that the MSTIDs propagating meridionally (equatorward and/or poleward) has lower velocity compared to those propagating zonally (eastward and/or westward). However, there is a distinct imbalance in the number of zonally and meridionally propagating MSTIDs, therefore, comparison may provide biased results. We have thus performed the significance test (Fisher Exact test) for the obtained results. [Fisher Exact test is a statistical procedure to determine the probabilities \(p value\) of categorical variables \(Fisher, 1935\), which works with the initial consideration that categories are independent. In the present study, we have used this test between two categories \(meridionally and zonally propagating MSTIDs\) and we found that differing velocities of zonally and meridionally propagating MSTIDs is significant \(p value < 0.0001\).](#) Table 1 also shows the dominant parameters (velocity range, period range, and azimuth angle) of the MSTIDs during all the four years. In addition, we have also assessed the characteristics with respect to seasons, however, we did not find any significant dependency on seasons observed in their occurrence (figure not provided).

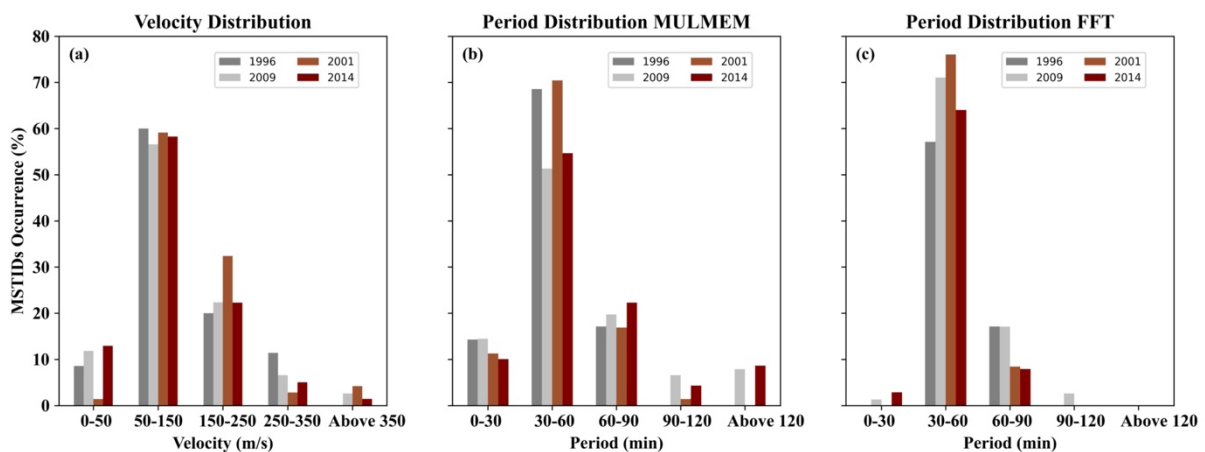


Figure 5. Velocity and period distribution of the MSTIDs observed during the four years of the two solar cycles.

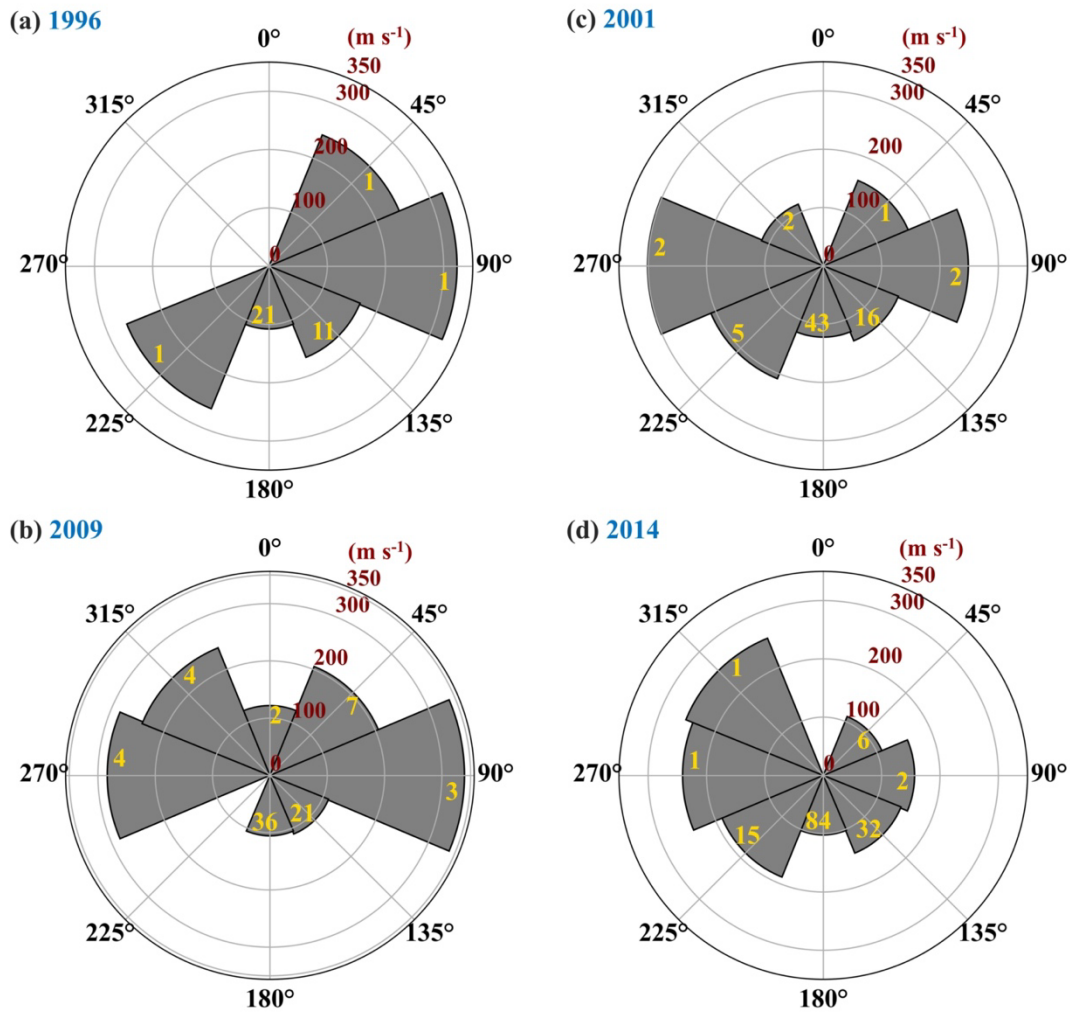


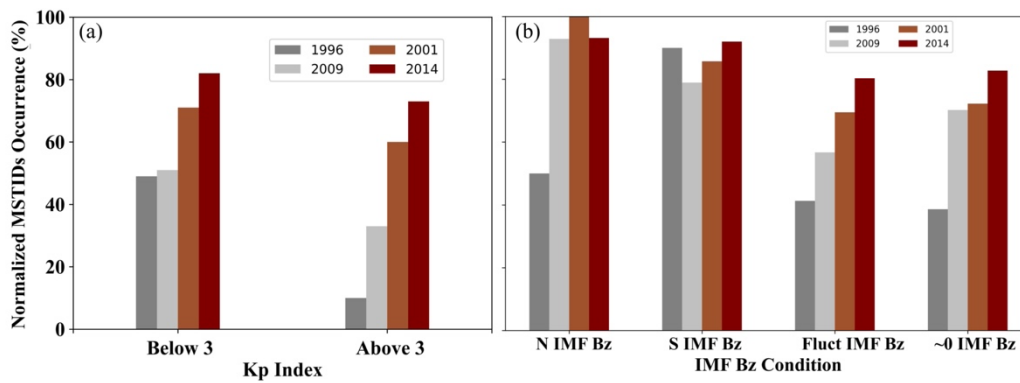
Figure 6. Distribution of the azimuth angle of MSTIDs, number of MSTIDs in each azimuth range (yellow values), and their average velocity (radial axis, labelled with red values).

Table 1. Showing the year wise MSTIDs' percentage occurrence (detected by MULMEM and total observed in the RT plots) and their dominant characteristics (velocity, period, & azimuth).

Year (solar activity)	Yearly Occurrence (%)		Dominant Vel. (m s ⁻¹)	Dominant Period (min)	Dominant Prop. Direc.
	Detected by MULMEM	Total (in RT plots)			
1996 (min)	~ 19	~ 41	50 – 150	30 – 60	Equatorward
2009 (min)	~ 25	~ 50	50 – 150	30 – 60	Equatorward
2001 (max)	~ 46	~ 72	50 – 150	30 – 60	Equatorward
2014 (max)	~ 47	~ 72	50 – 150	30 – 60	Equatorward

3.3. Solar wind driver and geomagnetic activity dependence of MSTIDs

255 We have further investigated the MSTID occurrence with respect to different Kp index levels and IMF Bz conditions, shown in Figure 7. We grouped the MSTIDs with respect to Kp; with $K_p \geq 3$ (geomagnetically active times) and $K_p < 3$ (geomagnetically quiet times). Their normalized percentage occurrence (obtained by dividing the number of MSTIDs in each Kp group to the total number of days within the respective group) is presented in Figure 7a. In both the categories, the occurrence of the MSTIDs is comparatively high during solar maximum years, consistent with their occurrence having a direct dependency on solar activity. [In order to check the variability of MSTID occurrence with respect to IMF Bz conditions, we segregated and normalized the MSTIDs into four groups designated as close to zero, prolonged northward, prolonged southward, and fluctuating IMF Bz. The segregation is done based on its behaviour in the considered time window of 8-16 UT with the following criteria: If the temporal average and standard deviation \(std\) of IMF Bz is within \$\pm 1.5nT\$, it is considered as 'close to zero'. For 'prolonged northward', if the temporal average is greater than \$1.5nT\$ with 80% of the IMF Bz values lying northward \(\$> 1.5nT\$ \) and remaining northward for at least two hours or more. For 'prolonged southward', if the temporal average is less than \$-1.5nT\$ with 80% of the IMF Bz values lying southward \(\$< -1.5nT\$ \) and remaining southward for at least two hours or more. For 'fluctuating IMF', the temporal average and std of IMF Bz is within \$\pm 2nT\$ and more than \$\pm 1.5nT\$ respectively with IMF Bz continuously fluctuating between north and south.](#) The normalization is done by dividing the number of MSTIDs in a particular IMF Bz category to the total number of days within the respective category for each year. Figure 7b shows the distribution of the normalized MSTID occurrence (%) with respect to each category. It is evident that irrespective of the categories of IMF Bz, MSTID occurrence is higher during solar maximum than during minimum years (Figure 7b and Table 2). It is interesting to note that MSTID occurrence is comparatively high during prolonged northward and southward IMF Bz conditions (excepting the 1996 minimum). During solar maximum years intervals of steady Bz conditions has more than 80% MSTID occurrence (100% during the 2001 maximum). Fisher exact significance test ([applied on the number of MSTIDs under maximum and minimum year categories](#)) also confirms the results are significant with p value less than 0.05. Small Bz or fluctuating Bz conditions tended to yield relatively few MSTIDs.



280 **Figure 7.** (a) Shows the distribution of the MSTIDs normalized with respect to Kp index. (b) Shows the distribution of the MSTIDs normalized with respect to different IMF Bz conditions.

Table 2. MSTIDs' normalized percentage occurrence with respect to Kp index and IMF Bz.

Year (solar activity)		1996 (min)	2009 (min)	2001 (max)	2014 (max)
Normalized Occurrence	$K_p < 3$	~ 49	~ 51	~ 71	~ 82

wrt Kp (%)	Kp > 3	~ 10	~ 30	~ 60	~ 73
Normalized Occurrence wrt IMF Bz (%)	Prolonged N	<u>~ 50</u>	<u>~ 93</u>	<u>~ 100</u>	<u>~ 93</u>
	Prolonged S	<u>~ 90</u>	<u>~ 79</u>	<u>~ 86</u>	<u>~ 92</u>
	Fluctuating	<u>~ 41</u>	<u>~ 57</u>	<u>~ 69</u>	<u>~ 80</u>
	Close to 0	<u>~ 38</u>	<u>~ 70</u>	<u>~ 72</u>	<u>~ 82</u>

285 We have further checked the variability of the MSTIDs' parameters with respect to different Kp index and IMF Bz conditions. The parameters do not show any variability with different Kp index conditions (figure not provided). Figure 8 shows the MSTIDs' average parameters (velocity, azimuth angle, and period) for different IMF Bz conditions during solar maximum (maroon curve) and minimum (grey curve) years. The parameters do not show significant variability with respect to solar activity and IMF Bz conditions. There is a relatively high velocity under steady IMF Bz (Northward and Southward) conditions during solar maximum years (Figure 8a). It is also noted that average values of the parameters in each IMF Bz category of solar max years are within 1 σ values (shown by error bars) of the solar min years and vice-versa and in the dominant parameter ranges as shown in Figures 5 & 6 and Table 1.

290

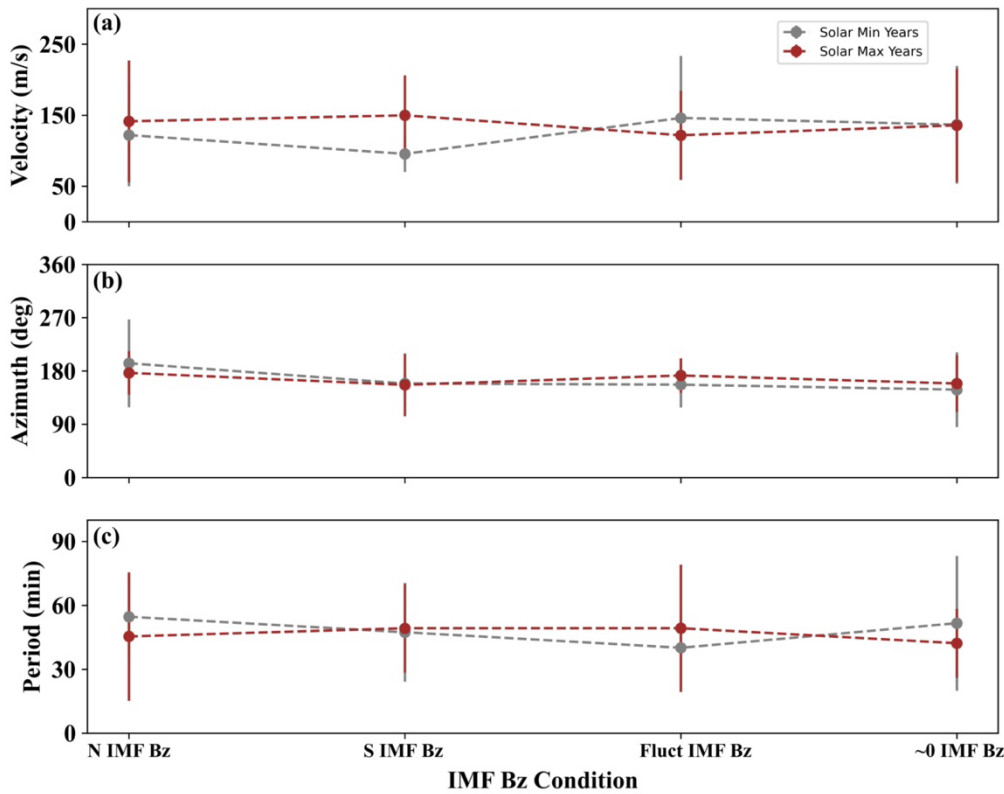


Figure 8. Shows the variability of the MSTIDs' average parameters during solar maximum (maroon curves) and minimum (grey curves) years under different IMF Bz conditions.

295 **4. Discussion**

In the previous section, we have described the characteristics and occurrence of high-latitude MSTIDs observed over the EISCAT 3D site location and how they vary with different levels of solar activity and with season. We can infer that most of the MSTIDs propagates equatorward (southward) with dominant velocity in the range of 50

– 150 m s⁻¹ and period in the range of 30 – 60 minutes. Their occurrence shows seasonal variation; they normally occur during winter and equinoctial months. We have also observed that with increasing solar activity the MSTID occurrence increases (Figure 4 & Table 1). In this section we discuss the role of solar forcing in the generation of MSTIDs. In addition, we also compare the results obtained by the MULMEM and FFT method.

4.1 Drivers behind the generation of high-latitude MSTIDs

Daytime high-latitude MSTIDs are analysed to examine their occurrence and possible generating sources. While previous works have reported their seasonal variations and proposed several generation mechanisms (such as geomagnetic forcing and atmospheric gravity waves), the dominant source remains uncertain. We investigated their occurrence with respect to different seasons and solar activity conditions. Our observations show a clear seasonal variation (Figure 4), with occurrence highest during winter and equinoctial months and lower during summer. [This pattern agrees with earlier reports of winter maxima at high latitudes \(Moges et al., 2024a; Negale et al., 2018; Ogawa et al., 1987\) and contrasts with summer peaks found in other studies \(e.g. Vlasov et al., 2011\). These studies investigated MSTIDs occurrence utilizing datasets from different instruments such as ionosonde, incoherent scatter radars, NNSS \(Navy Navigation Satellite System\) satellites, etc.](#) The similarity between the present seasonal pattern and that of atmospheric gravity wave activity in the Arctic (Hei et al., 2008; Hoffmann et al., 2010; Yoshiki & Sato, 2000) suggests that gravity waves propagating upward from the lower atmosphere may contribute to MSTIDs generation. However, the transmission of such waves is influenced by stratospheric and mesospheric filtering (Boyde et al., 2025) and possible dissipation at critical levels (Fritts & Vadas, 2008; Vadas, 2007). Confirmation of their role will require dedicated ray-tracing studies to identify specific sources and propagation paths.

In addition to the seasonal variation, MSTIDs occurrence also varies with solar activity (Figure 4c, Table 1), increasing from below 50% during solar minima to more than 70% during solar maxima. This behaviour broadly reflects the enhanced geomagnetic activity associated with higher solar flux. Previous studies have disagreed on the extent of geomagnetic control – some linking MSTIDs to Joule heating from storms and substorms (Prikryl et al., 2022, 2024), others noting frequent events during geomagnetically quiet times (Frissell et al., 2016; Ishida et al., 2008). Recently, Moges et al. (2024b) investigated MSTIDs amplitude-solar activity dependence and suggested that over high-latitudes the dependency is quite complex involving multiple mechanisms together. Our results show that the occurrence of high-latitude MSTIDs increases with increasing solar activity. We have further investigated their occurrence with respect to different Kp index levels (Figure 7a). However, there is a modest increase in their occurrence during geomagnetic quiet times (Kp < 3), even during solar maximum year, suggesting that Kp alone is not a good indicator of MSTIDs occurrence. This implies that there are other factors/sources that might be responsible for their generation.

[Recently, Xiong et al. \(2025\) reported an interesting case of daytime high-latitude MSTIDs during a geomagnetic quiet period of prolonged northward IMF Bz suggesting that Joule heating due to intermittent lobe reconnection can also be a possible factor for their generation. To explore the influence of IMF orientation, we have examined the role of different IMF Bz conditions \(prolonged northward, southward, fluctuating, and close to zero IMF Bz\) in the generation of the MSTIDs \(Figure 7b, Table 2\). Comparatively higher occurrence is observed during solar maximum years across all IMF Bz categories. Interestingly, the occurrence is highest \(more than 80 %\) during intervals of steady Bz conditions \(prolonged northward and southward\). This may reflect](#)

340 [MSTIDs occurrence being linked to enhanced Joule heating due to magnetic reconnection at the low-latitude magnetopause \(during southward IMF Bz\) and with the lobes \(during northward IMF Bz\). However, to comprehensively explore the role of different IMF Bz conditions in the generation of MSTIDs, a stand-alone study is needed.](#)

345 MSTID parameters do not show significant variation with respect to seasons, Kp index, IMF Bz conditions, and solar activity, implying that these factors primarily influence MSTIDs occurrence rate rather than their characteristics. [As discussed above, previous studies have used different datasets to investigate the climatology of high-latitude MSTIDs. Some studies have reported their characteristics, others have mentioned the complex dependency of their amplitude on solar activity, and a few have reported their seasonal variations \(Moges et al., 2024a & 2024b; Negale et al., 2018; Ogawa et al., 1987; Vlasov et al., 2011\). The present study encompasses not only the characteristics and seasonal variation but also reports their dependency on IMF Bz configurations and solar activity.](#) Overall, our findings indicate that both internal atmospheric processes and external solar forcing contribute to MSTIDs generation. The relative dominance of these mechanisms remains uncertain, but the present statistical analysis helps constrain their roles and provides guidance for scheduling future experimental runs of EISCAT-3D to explore in-depth the MSTIDs with 3-dimensional structures.

355 **4.2 Comparison of MULMEM & FFT results: A need for multi-instrument and multi-method studies**

As explained above, the MULMEM analysis does not always return a result, so we have also computed the MSTID periods using FFT. [We have compared the period of the observed MSTIDs from both methods and found some discrepancies, as seen in two cases with differing results as presented in Figures 3 & 9.](#) The period of the MSTID determined using the two methods in Figure 3 are nearly the same, whereas the period determined in the second case (see Figure 9) is different between 12 and 14 UT. Figure 9a (RT plot) implies that the time separation of the MSTID bands in this case was less than 60 minutes between 9 and 13 UT with a higher time separation (~90 minutes) between 13 and 15 UT. This is consistent with the period determined using FFT (see blue curve in Figure 9b). The period determined using the MULMEM (see red curve in Figure 9b) is more than 120 minutes. [We can infer from these results that MULMEM overestimated the period in this case. This might be due to the approach used by MULMEM. In MULMEM there is automatic selection of the time series, which could result in certain selections where MSTID structure was not prominent, and hence skipping of some MSTID bands.](#) On the other hand, in the FFT method we have manually selected the time series where the MSTID bands were prominent in the RT plots to determine the period. To further investigate any disparity in the results, we have compared the average period of all the observed MSTIDs during the four years using both FFT and MULMEM, shown in Figure 360 10. The red curve shows the average period determined using MULMEM and the blue shows the average period using FFT of each MSTID event. The period determined using both the methods generally shows quite similar values, however there are a few cases during 2009 and 2014 where MULMEM overestimated the period (Figures 370 10c-d).

375 [These results assess the performance of MULMEM in the detection and parameter estimation of MSTIDs. The performance of MULMEM in detecting MSTIDs can be seen from Table 1 where the success rate of MULMEM hovered between 50-60% with respect to MSTID events observed in RT plots. We have also assessed its performance in determining the MSTIDs' parameters. We find that MULMEM has estimated a similar period to the FFT \(standard deviation < 20% of the mean period\) in more than 75% of cases. There are a few cases where](#)

380
385

it has underestimated/overestimated the period and in most of those cases the performance reduced due to weak (average GBS ≤ 15 dB) or noisy (continuous GBS between the MSTID bands) signals. It is also worth noting that the results in this study are based on a single dataset of GBS observations from the HAN radar, which itself shows a seasonal variation. Despite our efforts to account for the variation in GBS, it is nevertheless difficult to rule out the possibility that the seasonal variations and mischaracterization of the MSTIDs parameters might have some additional biases incurred due to observational constraints and inefficiency of the analytical method. Therefore, future studies will employ a multi-instrument and multi-method approach to mitigate any such biases in the observations.

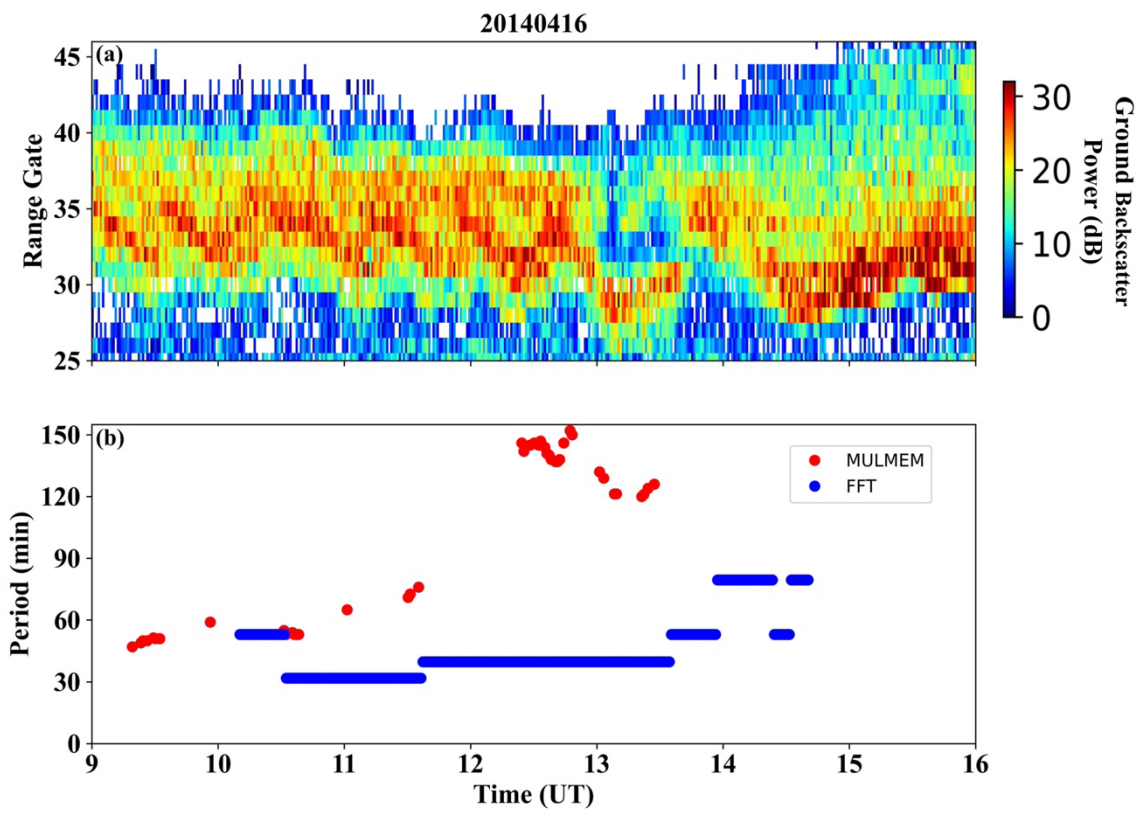
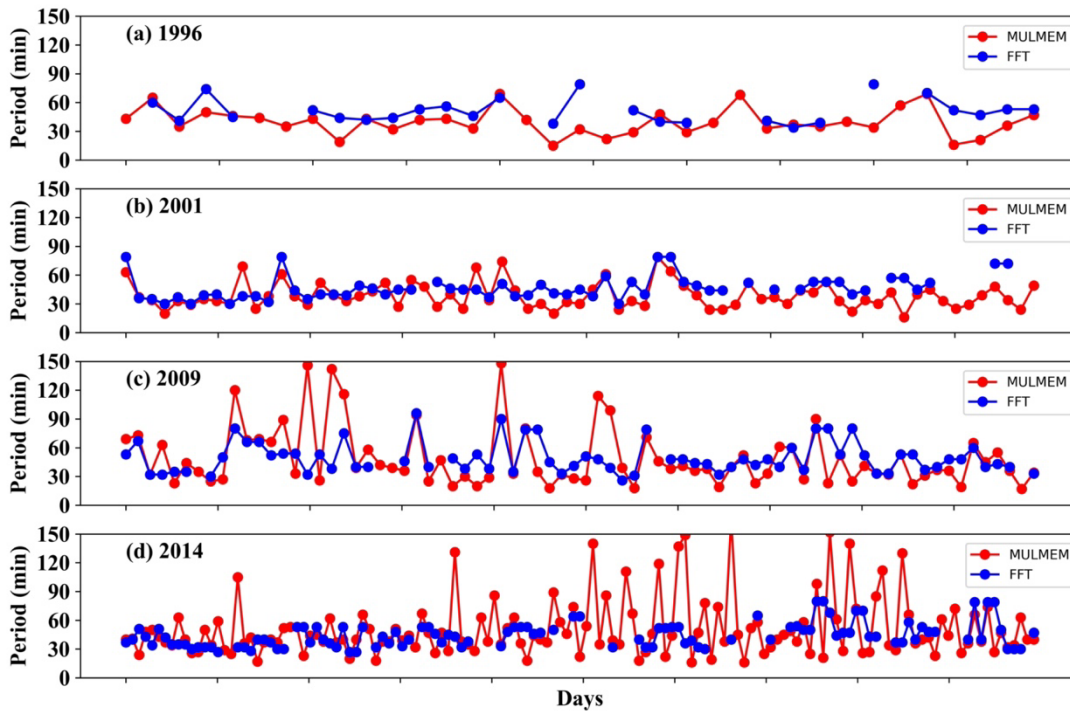


Figure 9. (a) RT plot shows an example of the MSTIDs. (b) Period of the observed MSTID derived using MULMEM (red curve) and FFT (blue curve).



390 **Figure 10.** Shows the comparison of the period of MSTIDs (observed across all four years) derived using
 395 MULMEM (red curve) and FFT (blue curve) method.

5. Conclusions

This study has presented a statistical overview of high-latitude MSTIDs over the newly established EISCAT-3D
 395 radar site. To explore the characteristics and generating sources, ground backscatter data from the Hankasalmi
 radar during solar maximum (2001 & 2014) and minimum (1996 & 2009) years of solar cycles 23 and 24 have
 been used. The primary population of MSTIDs propagates equatorward with velocity and period in the range of
 50 – 150 m s⁻¹ and 30 – 60 minutes, respectively. Their occurrence shows seasonal (primary peaks during winter
 and equinoctial months) as well as solar activity dependency (significantly higher occurrence (~72%) during solar
 400 maximum years). Furthermore, their occurrence shows little dependence on Kp index; irrespective of the Kp index
 conditions, it increases with increasing solar activity. It is interesting to note that MSTIDs show a comparatively
 high occurrence during prolonged northward and southward IMF Bz conditions with more than 80% during solar
 maximum years. This increment in the MSTIDs occurrence might be due to the enhanced Joule heating caused
 by magnetic reconnection, either at the low-latitude or lobe magnetopause, during these IMF Bz conditions. It is
 405 interesting to note that their parameters (velocity, azimuth, and period) do not show any significant variability
 with respect to seasons, Kp index, IMF Bz conditions, and solar activity. This study tries to elicit the role of
 different sources (solar activity, geomagnetic activity, IMF Bz) on the generation of high-latitude MSTIDs but
 there still exists uncertainty regarding the dominant drivers. Also, in the determination of the characteristics using
 the MULMEM method an inconsistency has been observed, which necessitates a future study using a multi-
 410 instrument and multi-method approach.

Data Availability / Open Data. Data were obtained from the SuperDARN data mirror at the British Antarctic Survey (<https://api.bas.ac.uk/superdarn/mirror/v3/>). The data were processed utilizing the FITACF 2.5 library from the Radar Software Toolkit (RST; SuperDARN Data Analysis Working Group, 2025) and pyDARN python library (SuperDARN Data Visualization Working Group, 2025).

Author Contributions. AG and RR conceptualized the idea, performed analyses, and wrote the original manuscript. TKY and ML reviewed and edited the manuscript.

Competing interests. The authors declare no conflicts of interest relevant to this study.

Acknowledgements. RR and AG acknowledge the financial support from the UKRI NERC funded project NE/W003090/1. TKY is supported by UKRI STFC Grant ST/S000429/1 and NERC grant NE/V000748/1. ML is supported by UKRI STFC Grant ST/S000429/1. The authors acknowledge the use of SuperDARN data. SuperDARN is a collection of radars funded by national scientific funding agencies of Australia, Canada, China, France, Italy, Japan, Norway, South Africa, United Kingdom, and the United States of America. The Hankasalmi radar is maintained and operated by University of Leicester with current support from UKRI NERC under NE/V000748/1.

References:

- 430 Boyde, B., Wood, A., Dorrian, G., Fallows, R. A., Themens, D., Mielich, J., et al.: Lensing from small-scale travelling ionospheric disturbances observed using LOFAR, *Journal of Space Weather and Space Climate*, 12, 34, <https://doi.org/10.1051/swsc/2022030>, 2022.
- Boyde, B., Wood, A., Dorrian, G., de Gasperin, F., Mevius, M.: Statistics of travelling ionospheric disturbances observed using the LOFAR radio telescope, *Journal of Space Weather and Space Climate*, 15, 6, 435 <https://doi.org/10.1051/swsc/2025002>, 2025.
- Carter, B. A., Pradipta, R., Dao, T., Currie, J. L., Choy, S., Wilkinson, P., et al.: The ionospheric effects of the 2022 Hunga Tonga Volcano eruption and the associated impacts on GPS Precise Point Positioning across the Australian region, *Space Weather*, 21, e2023SW003476, <https://doi.org/10.1029/2023SW003476>, 2023.
- 440 Chisham, G., Lester, M., Milan, S.E., Freeman, M. P., Bristow, W. A., Grocott, A., et al.: A decade of the Super Dual Auroral Radar Network (SuperDARN): scientific achievements, new techniques and future directions. *Surveys in Geophysics*, 28, 33–109, <https://doi.org/10.1007/s10712-007-9017-8>, 2007.
- Ding, F., Wan, W., Liu, L., Afraimovich, E. L., Voeykov, S. V., & Perivalova, N. P.: A statistical study of large-scale traveling ionospheric disturbances observed by GPS TEC during major magnetic storms over the years 2003 – 2005, *Journal of Geophysical Research*, 113, A00A01, <https://doi.org/10.1029/2008JA013037>, 2008.
- 445 Ding, F., Wan, W., Xu, G., Yu, T., Yang, G., & Wang, J.: Climatology of medium-scale traveling ionospheric disturbances observed by a GPS network in central China, *Journal of Geophysical Research*, 116, A09327, <https://doi.org/10.1029/2011ja016545>, 2011.
- [Fisher, R. A. The logic of inductive inference. *Journal of the Royal Statistical Society*, 98, pp. 39-82, <https://doi.org/10.2307/2342435>, 1935.](https://doi.org/10.2307/2342435)
- 450 Frissell, N. A., Baker, J. B., Ruohoniemi, J. M., Greenwald, R. A., Gerrard, A. J., Miller, E. S., & West, M. L.: Sources and characteristics of medium-scale traveling ionospheric disturbances observed by high-frequency radars in the North American sector, *Journal of Geophysical Research: Space Physics*, 121(4), 3722–3739, <https://doi.org/10.1002/2015JA022168>, 2016.
- 455 Fritts, D. C. & Vadas, S. L.: Gravity wave penetration into the thermosphere: sensitivity to solar cycle variations and mean winds, *Annales Geophysicae*, 26, 3841–3861, <https://doi.org/10.5194/angeo-26-3841-2008>, 2008.
- Greenwald, R. A., Baker, K. B., Dudeney, J. R., Pinnock, M., Jones, T. B., Thomas, E. C., et al.: Darn/SuperDarn: A global view of the dynamics of high-latitude convection, *Space Science Reviews*, 71, 761–796, <https://doi.org/10.1007/BF00751350>, 1995.
- 460 Grocott, A., K. Hosokawa, T. Ishida, M. Lester, S. E. Milan, M. P. Freeman, N. Sato, and A. S. Yukimatu: Characteristics of medium-scale traveling ionospheric disturbances observed near the Antarctic Peninsula by HF radar, *Journal of Geophysical Research: Space Physics*, 118, 5830–5841, <https://doi.org/10.1002/jgra.50515>, 2013.
- Hines, C. O.: Internal atmospheric gravity waves at ionospheric heights, *Canadian Journal of Physics*, 38(11), 1441–1481, <https://doi.org/10.1139/p60-150>, 1960.
- 465 Hocke, K., & Schlegel, K.: A review of atmospheric gravity waves and travelling ionospheric disturbances: 1982–1995, *Annales Geophysicae*, 14(9), 917, <https://doi.org/10.1007/s005850050357>, 1996.
- Huang, F., Dou, X., Lei, J., Lin, J., Ding, F., & Zhong, J.: Statistical analysis of nighttime medium-scale traveling ionospheric disturbances using airglow images and GPS observations over central China, *Journal of Geophysical Research: Space Physics*, 121(9), 8887–8899, <https://doi.org/10.1002/2016ja022760>, 2016.
- 470 Hunsucker, R. D.: Atmospheric gravity waves generated in the high latitude ionosphere: A review, *Reviews of Geophysics*, 20(2), 293–315, <https://doi.org/10.1029/rg020i002p00293>, 1982.

- Ishida, T., Hosokawa, K., Shibata, T., Suzuki, S., Nishitani, N., & Ogawa, T.: SuperDARN observations of daytime MSTIDs in the auroral and mid-latitudes: Possibility of long-distance propagation, *Geophysical Research Letters*, 35(13), L13102, <https://doi.org/10.1029/2008gl034623>, 2008.
- 475 Maletckii, B., & Astafyeva, E.: Near-real-time identification of the source of ionospheric disturbances, *Journal of Geophysical Research: Space Physics*, 129, e2024JA032664, <https://doi.org/10.1029/2024JA032664>, 2024.
- Milan, S.E., Yeoman, T.K., Lester, M., Thomas, E. C., & Jones, T. B.: Initial backscatter occurrence statistics from the CUTLASS HF radars, *Annales Geophysicae*, 15, 703–718, <https://doi.org/10.1007/s00585-997-0703-0>, 1997.
- 480 [Moges, S. T., Sherstyukov, R. O., Kozlovsky, A., Ulich, T., & Lester, M.: Statistics of traveling ionospheric disturbances at high latitudes using a rapid-run ionosonde, *Journal of Geophysical Research: Space Physics*, 129, e2023JA031694, <https://doi.org/10.1029/2023JA031694>, 2024a.](#)
- Moges, S. T., Kozlovsky, A., Sherstyukov, R. O., & Ulich, T.: Solar activity dependence of traveling Ionospheric disturbance amplitudes using a rapid-run ionosonde in high latitudes, *Journal of Geophysical Research: Space Physics*, 129, e2024JA033013, <https://doi.org/10.1029/2024JA033013>, 2024b.
- 485 Negale, M. R., Taylor, M. J., Nicolls, M., Vadas, S. L., Nielsen, K., & Heinselman, C. J.: Seasonal propagation characteristics of MSTIDs observed at high latitudes over central Alaska using the poker flat incoherent scatter radar, *Journal of Geophysical Research: Space Physics*, 123(7), 5717–5737, <https://doi.org/10.1029/2017ja024876>, 2018.
- 490 Ogawa, T., Igarashi, K., Aikyo, K., & Maeno, H.: NNSS Satellite-observations of medium-scale traveling ionospheric disturbances at southern high-latitudes, *Journal of Geomagnetism and Geoelectricity*, 39(12), 709–721, <https://doi.org/10.5636/jgg.39.709>, 1987.
- Prikryl, P., Gillies, R. G., Themens, D. R., Weygand, J. M., Thomas, E. G., & Chakraborty, S.: Multi-instrument observations of polar cap patches and traveling ionospheric disturbances generated by solar wind Alfvén waves coupling to the dayside magnetosphere, *Annales Geophysicae*, 40(6), 619–639, <https://doi.org/10.5194/angeo-40-619-2022>, 2022.
- 495 Prikryl, P., Themens, D. R., Chum, J., Chakraborty, S., Gillies, R. G., & Weygand, J. M.: Observations of traveling ionospheric disturbances driven by gravity waves from sources in the upper and lower atmosphere, *Annales Geophysicae*, 43, 511–534, <https://doi.org/10.5194/angeo-43-511-2025>, 2025.
- 500 Rathi, R., Sivakandan, M., Chakraborty, D., Sunil Krishna, M.V., Upadhayaya, A.K., Sarkhel, S.: Evidence for the evolution and decay of an electrified medium scale traveling ionospheric disturbances during two consecutive substorms: First results, *Advances in Space Research*, 75, 6, <https://doi.org/10.1016/j.asr.2025.01.007>, 2025.
- Samson, J., Greenwald, R., Ruohoniemi, J., & Baker, K.: High-frequency radar observations of atmospheric gravity waves in the high-latitude ionosphere, *Geophysical Research Letters*, 16(8), 875–878, <https://doi.org/10.1029/gl016i008p00875>, 1989.
- 505 Samson, J., Greenwald, R., Ruohoniemi, J., Frey, A., & Baker, K.: Goose bay radar observations of Earth-reflected, atmospheric gravity waves in the high-latitude ionosphere, *Journal of Geophysical Research*, 95(A6), 7693–7709, <https://doi.org/10.1029/ja095ia06p07693>, 1990.
- Shibata, T.: Application of multichannel maximum-entropy spectral-analysis to the HF Doppler data of medium-scale TID, *Journal of Geomagnetism and Geoelectricity*, 39(5), 247–260, <https://doi.org/10.5636/jgg.39.247>, 1987.
- 510 Shiokawa, K., Ihara, C., Otsuka, Y., & Ogawa, T.: Statistical study of nighttime medium-scale traveling ionospheric disturbances using midlatitude airglow images, *Journal of Geophysical Research*, 108(A1), <https://doi.org/10.1029/2002ja009491>, 2003.

- 515 Shiokawa, K., Mori, M., Otsuka, Y., Oyama, S., Nozawa, S., Suzuki, S., & Connors, M.: Observation of nighttime medium-scale traveling ionospheric disturbances by two 630 nm airglow imagers near the auroral zone, *Journal of Atmospheric and Solar-Terrestrial Physics*, 103, 184–194, <https://doi.org/10.1016/j.jastp.2013.03.024>, 2013.
- Strand, O. N.: Multichannel complex maximum entropy (autoregressive) spectral analysis, *IEEE Transactions on Automatic Control*, 22(4), 634–640, <https://doi.org/10.1109/TAC.1977.1101545>, 1977.
- 520 SuperDARN Data Visualization Working Group, Martin, C. J., Rohel, R. A., Billett, D. D., Pitzer, P., Galeshuck, D., Kunduri, B. S. R., Khanal, K., Hiyadutuje, A., Chakraborty, S., Detwiler, M., & Schmidt, M. T.: SuperDARN/pydarn: pyDARN v4.1.2 (v4.1.2), Zenodo, <https://doi.org/10.5281/zenodo.15441879>, 2025.
- SuperDARN Data Analysis Working Group, Thomas, E. G., Burrell, A. G., Ponomarenko, P. V., Bland, E. C., Sterne, K. T., Rohel, R. A., Shepherd, S. G., Billet, D. D., Schmidt, M. T., & Walach, M.-T.: SuperDARN Radar Software Toolkit (RST) 5.1 (v5.1), Zenodo, <https://doi.org/10.5281/zenodo.4435150>, 2025.
- 525 Tsugawa, T., Saito, A., & Otsuka, Y. (2004). A statistical study of large-scale traveling ionospheric disturbances using the GPS network in Japan. *Journal of Geophysical Research*, 109, A06302. <https://doi.org/10.1029/2003JA010302>
- Ulrych, T. J., & T. N. Bishop: Maximum entropy spectral analysis and autoregressive decomposition, *Reviews of Geophysics*, 13(1), 183–200, <https://doi.org/10.1029/RG013i001p00183>, 1975.
- 530 Vadas, S. L.: Horizontal and vertical propagation and dissipation of gravity waves in the thermosphere from lower atmospheric and thermospheric sources, *Journal of Geophysical Research*, 112(A6), A06305, <https://doi.org/10.1029/2006JA011845>, 2007.
- Vlasov, A., Kauristie, K., van de Kamp, M., Luntama, J.-P., and Pogoreltsev, A.: A study of Traveling Ionospheric Disturbances and Atmospheric Gravity Waves using EISCAT Svalbard Radar IPY-data, *Annales Geophysicae*, 29, 2101–2116, <https://doi.org/10.5194/angeo-29-2101-2011>, 2011.
- 535 Xiong, Y., Liu, H., Shi, R., Xing, Z., Lu, S., Zhang, Q., et al.: Generation of quasi-periodic dayside medium scale traveling ionospheric disturbances (MSTIDs) by intermittent lobe reconnection, *Geophysical Research Letters*, 52, e2024GL113857, <https://doi.org/10.1029/2024GL113857>, 2025.